Localized electron density engineering for stabilized B-γ $CsSnI_3$-based perovskite solar cells with efficiencies >10%

Tao Ye,[1]* Xizu Wang,[2] Kai Wang,[1] Shaoyang Ma,[3] Dong Yang,[1] Yuchen Hou,[1] Jungjin Yoon,[1] Ke Wang,[4] Shashank Priya[1]*

[1]Department of Materials Science and Engineering, Pennsylvania State University, University Park, PA 16802, USA

[2]Institute of Materials Research and Engineering (IMRE), Agency for Science, Technology and Research, #08-03, 2 Fusionopolis Way, Innovis, 138634, Singapore

[3]Key Laboratory of All Optical Network and Advanced Telecommunication Network of Ministry of Education, Institute of Lightwave Technology, Beijing Jiaotong University, Beijing 100044, China

[4]Materials Research Institute, Pennsylvania State University, University Park, PA 16802, USA

*Corresponding author. Email: tvy5161@psu.edu; sup103@psu.edu.

Abstract

Black orthorhombic (B-γ) $CsSnI_3$ with low toxicity and excellent optoelectronic properties is a promising candidate for perovskite solar cell (PSC). However, the performance of the B-γ $CsSnI_3$-based PSCs is much lower than their lead-based or

organotin-based counterparts due to the heavy self-doping of Sn^{2+} to form Sn^{4+} under ambient-air condition. Here, this undesirable oxidation in $CsSnI_3$ is restricted by engineering the localized electron density with phthalimide (PTM) additive. The lone electron pairs of NH and two CO units of PTM are designed to form trigeminal coordination bonding with Sn^{2+}, resulting in reduced defect density and relatively grain-ordered perovskite film. The champion efficiencies of 10.1% and 9.6% are obtained for the modified rigid and flexible B-γ $CsSnI_3$-based PSCs, respectively. These encapsulated devices maintain 94.3%, 83.4%, and 81.3% of their initial efficiencies under inert (60 days), ambient (45 days), and 1 Sun continuous illumination at ~70 ºC (2000 min) conditions, respectively.

TOC

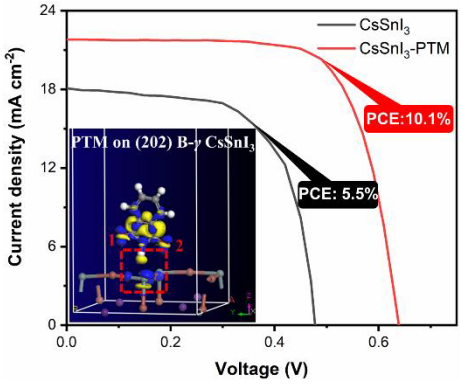

Intensive efforts have been invested in lead-free tin halide perovskite for solar cell fabrication due to its low toxicity and high theoretical power conversion efficiency (PCE).[1-3] One of the promising candidates within tin halide perovskite family is the fully-inorganic cesium tin triiodide ($CsSnI_3$).[4-6] This material can crystallize into two

different phases at room temperature: one-dimensional double-chain structure (Y $CsSnI_3$), a photoinactive phase; and a three-dimensional perovskite structure (B-γ), a desired photoactive phase.[7,8] The bandgap of ~1.31 eV for the B-γ $CsSnI_3$ at room temperature (RT) is located within the ideal bandgap range in which the PCE of a single-junction photovoltaic device can approach the Shockley-Queisser limit.[9] The low-cost solution process deposited B-γ $CsSnI_3$ also possesses excellent optoelectronic properties, including high optical absorption coefficient, low exciton binding energy, high charge mobilities, and high stability as compared to the organotin based perovskites.[4,5,10] Thus, high photocurrent can be generated within the B-γ $CsSnI_3$-based perovskite solar cells (PSCs). However, the photoactive B-γ $CsSnI_3$ is known to rapidly degrade to the yellow polymorph structure (Y $CsSnI_3$) and subsequently transfer to photoinactive Cs_2SnI_6 because of self-doping from Sn^{2+} to form Sn^{4+} under ambient-air conditions.[7,8] Thus, restricting undesirable oxidation from Sn^{2+} to Sn^{4+} is an efficient way for achieving high PCE and stable B-γ $CsSnI_3$ PSCs.[11]

B-γ $CsSnI_3$ was used as hole transport layer in an all-solid-state dye-sensitized solar cell, and a PCE as high as 10.2% was documented.[12] After that, a Schottky solar cell with a configuration of: indium tin oxide (ITO)/$CsSnI_3$/Au/Ti, has been fabricated and a PCE of 0.9% has been reported.[13] To reduce the self-doping from Sn^{2+} to Sn^{4+} (defect density) in the B-γ $CsSnI_3$ system, some methods have been implemented, such as optimization of charge carrier transport layer,[14] incorporation of additives[4,6,15-17] and manipulation[18] of dimensionality. However, the highest PCE of the resulting PSCs has

been limited to ~8%.[16] This value is much lower than that of the lead-based (25.5%)[19-21] or organotin-based (13.24%) PSCs[22-24]. Furthermore, the operational stability results on the B-γ $CsSnI_3$ devices have been rarely discussed in the literature. At this juncture, promising stabilization approaches that simultaneously enhance PCE and stability of B-γ $CsSnI_3$ PSCs are urgently required.

Here, we report on the localized electron density engineering through trigeminal coordination interactions between phthalimide (PTM) and B-γ $CsSnI_3$ to form a relatively grain-ordered, low defect density, and highly stable perovskite light absorber. Through systematically coupled theory and experiments, we demonstrate that the lone electron pairs of NH and two CO functional groups in the PTM form coordination interactions with Sn^{2+} in the $CsSnI_3$ and protect it from oxidation to Sn^{4+}. The highest PCEs of 10.1% and 9.6% are obtained for the rigid and flexible PTM modified PSCs, respectively. Further, we demonstrate that the PTM modified PSCs are highly stable under inert, ambient-air, and 1 Sun continuous illumination at 70 ^{o}C conditions for long periods.

Firstly, 3.0 mg (0.0068 mmol) PTM was fully dissolved in 1 mL of 0.8 M $CsSnI_3$ solutions (abbreviated as $CsSnI_3$-PTM, Supplementary Fig. 1). The perovskite films were deposited *via* a two-step spin-coating process and the chlorobenzene was used as an antisolvent[23,24] to obtain mirror-like surface of the perovskite films (Supplementary Fig. 2). For a solar cell, the bandgap of the light absorber is a critical factor. The bandgap

of the $CsSnI_3$-PTM is 1.31 eV, which is identical with that of the plain $CsSnI_3$ sample, as shown in the Tauc plots of optical absorption spectra in Fig. 1a. The emission properties of the as-prepared perovskite films on top of quartz substrates have been measured with steady-state photoluminescence (PL) spectroscopy, as presented in Fig. 1b. An enhanced PL peak can be found for the $CsSnI_3$-PTM sample as compared with its $CsSnI_3$ counterpart, indicating that lower defect density[25,26] was generated within the PTM modified $CsSnI_3$ sample after incorporation of PTM, which is consistent with the smaller Urbach energy of the $CsSnI_3$-PTM film (Supplementary Fig. 3). The PL peak intensity decreased with more PTM addition within the system, as the PL spectra shown in Supplementary Fig. 4. Supplementary Fig. 5 shows the time-resolved photoluminescence (TRPL) spectra of the $CsSnI_3$ and $CsSnI_3$-PTM samples and two PL lifetimes of each spectrum can be extracted accordingly (the fitting method are presented in Supplementary Note 1). The average PL decay lifetime was calculated to be 3.39 ns for the $CsSnI_3$ sample, where τ_1 and τ_2 were found to be 1.16 and 4.52 ns with A_1 and A_2 of 66.48% and 33.52%, respectively. After the incorporation of PTM, the average PL lifetime increased significantly to 11.97 ns, where τ_1 and τ_2 were increased to 5.00 and 16.04 ns with A_1 and A_2 of 65.20% and 34.80%, respectively (Supplementary Table 1). Typically, the fast lifetime component originates from the quenching of charge carriers at surface, while the slow lifetime component corresponds to the trap-induced non-radiative recombination of charge carriers within the bulk perovskite film[25,26]. Therefore, the defect density in the $CsSnI_3$-PTM sample was much decreased as compared to its $CsSnI_3$ counterpart.

The grazing incidence X-ray diffraction (GIXRD) patterns of as-prepared $CsSnI_3$ and $CsSnI_3$-PTM films are shown in Fig. 1c. Both perovskite samples exhibited typical XRD pattern corresponding to a B-γ $CsSnI_3$ structure (the simulated XRD pattern of B-γ $CsSnI_3$ is shown in Supplementary Fig. 6).[7,27] After the addition of PTM, the peak intensity of [101] facets was remarkably enhanced but the peak intensity of (220) and (022) facets was reduced when compared to the simulated and plain $CsSnI_3$ samples. This indicates that the relatively ordered arrangement of the $CsSnI_3$ grains arises from the interactions between the PTM and perovskite.[28,29] These relatively ordered crystal grains will reduce the surface area of the grain boundaries and further improve the charge carrier transport[25,30] within the $CsSnI_3$-PTM film, resulting in higher performance of photovoltaic devices.

The surface morphology of the perovskite films was investigated using scanning electron microscopy (SEM), as shown in Fig. 1d and 1e. Both samples exhibited smooth surface except for minor pits were found on the surface of bare $CsSnI_3$ sample, which may increase non-radiative recombination.[22,31] However, over addition of PTM may decrease the grain size (Supplementary Fig. 7), resulting in more grain boundaries in the perovskite film and thereby reducing the charge carrier transport (Supplementary Fig. 4) and device performance.[26] To characterize the nanostructure of as-deposited perovskite samples, high-resolution transmission electron microscopy (HRTEM) has been conducted and the results are shown in Figs. 1f and 1g (the images without marks

are shown in Supplementary Figs. 8 and 9). With regards to plain $CsSnI_3$ sample, the d-spacing value was 0.31 nm, which corresponds to the (202) facet of B-γ $CsSnI_3$ (the simulated d-spacing values of different B-γ $CsSnI_3$ facets can be seen in Supplementary Table 2). In case of the $CsSnI_3$-PTM sample (Fig. 1g), the ~1.2 nm thick layer of PTM was found to cover the crystalline $CsSnI_3$ grain in the $CsSnI_3$-PTM sample (forming a core-shell structure). The clearer lattice fringes of perovskite crystal grain could be found in the $CsSnI_3$-PTM sample, indicating that higher crystallinity of the perovskite grains. The high crystallinity will decrease the non-radiative charge carrier recombination[28,30] within the $CsSnI_3$-PTM film, leading to enhanced performance of PSCs. This is also confirmed by the energy dispersive X-ray (EDS) elemental mapping in Supplementary Fig. 10. Thus, the $CsSnI_3$-PTM material is a good candidate for PSC fabrication due to its proper bandgap, lower defect density, relatively ordered crystal grains, and high ambient-air stability.

Kelvin probe force microscopy (KPFM) measurements were conducted to characterize the electronic properties of $CsSnI_3$ before and after the addition of PTM, and the results are shown in Fig. 1h-1j. The contact potential difference (CPD) images of the pristine $CsSnI_3$ and $CsSnI_3$-PTM samples are presented with identical potential range in same color scale (Fig. 1h and 1i). CPD is a metrics of the potential difference between work function of sample surface (Φ_{sample}) and tip (Φ_{tip}), which is often used to calculate Fermi level of a sample (as illustrated in Supplementary Figs. 11-13 and Supplementary Note 2).[32,33] The Fermi level distribution of the two samples is shown in Fig. 1j, where the

Fermi levels were estimated to be -4.54 and -4.38 eV for the pristine $CsSnI_3$ and $CsSnI_3$-PTM samples, respectively. These results are consistent with the ultraviolet photoelectron spectroscopy (UPS) and optical absorption results (Fig. 1a) that the Fermi level of the $CsSnI_3$-PTM (-4.40 eV) is shallower than that of the $CsSnI_3$ (-4.52 eV), as illustrated in Supplementary Figs. 14 and 15, and Supplementary Note 3. It is widely reported[8,11,23] that the performance of tin halide perovskite films suffers from their p-type behavior due to the self-doping from Sn^{2+} to Sn^{4+} upon oxidation. The incorporation of PTM shifted the surface Fermi level of $CsSnI_3$ towards shallower value, indicating that the defects were passivated within the sample.

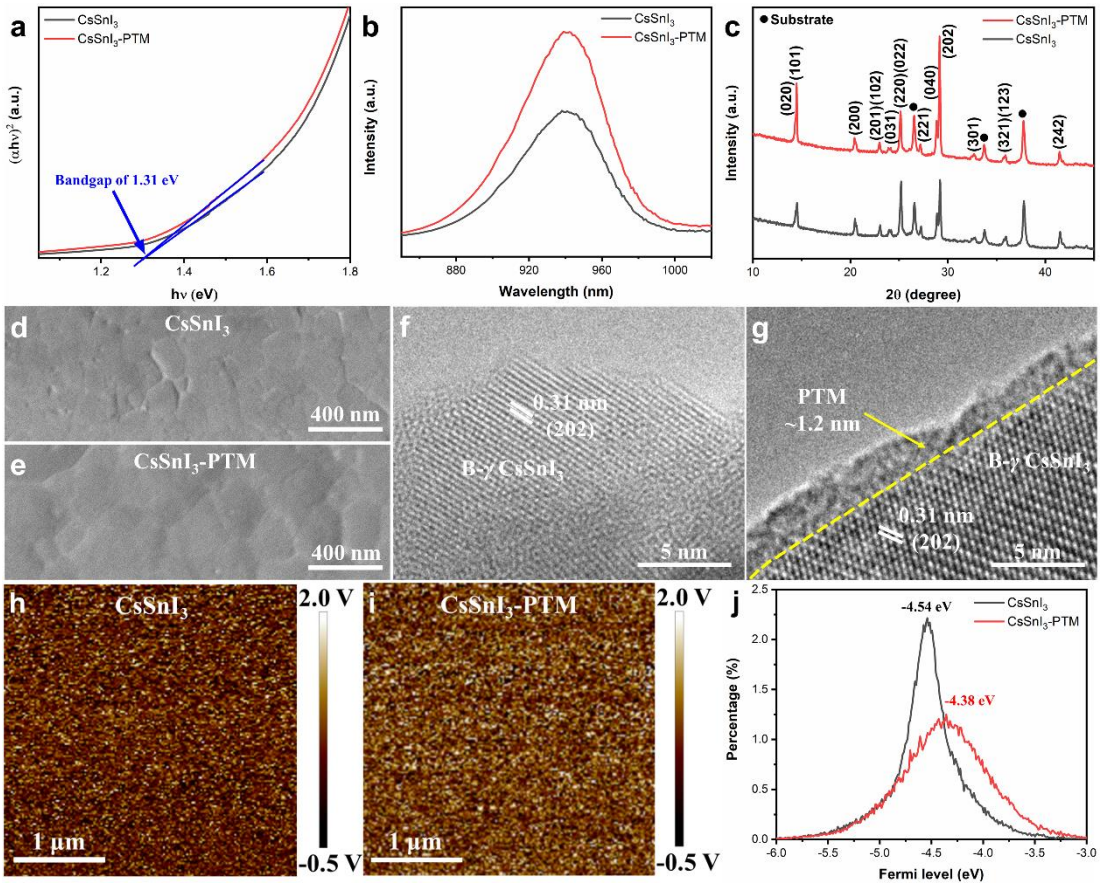

Fig. 1. Deposition of perovskite films. (**a**) Bandgaps of $CsSnI_3$ and $CsSnI_3$-PTM films

extracted from Tauc plots of the optical absorption spectra. (**b**) Steady-state PL spectra of $CsSnI_3$ and $CsSnI_3$-PTM samples, Xenon light was irradiated on the perovskite sample surface. (**c**) GIXRD patterns of the $CsSnI_3$ and $CsSnI_3$-PTM samples. Surface SEM images of the (**d**) $CsSnI_3$ and (**e**) $CsSnI_3$-PTM samples, respectively. (**f**) HRTEM image shows the lattice structure of the $CsSnI_3$ sample. (**g**) HRTEM image shows the coherent interface between PTM and $CsSnI_3$ within the $CsSnI_3$-PTM sample. Surface potential mapping features measured by KPFM method for (**h**) $CsSnI_3$ and (**i**) $CsSnI_3$-PTM samples, respectively. (**j**) Fermi level profiles of the $CsSnI_3$ and $CsSnI_3$-PTM films.

Thermo-gravimetric analysis (TGA) measurements[34] were conducted on $CsSnI_3$ and $CsSnI_3$-PTM samples, as shown in Supplementary Fig. 16. The PTM modified sample lost 4.1% of its initial weight at 152 ºC, while the loss of the pristine $CsSnI_3$ sample was 7.2% at 161 ºC. The initial stage of weight loss was originated from the sublimation of SnI_4,[35,36] so the addition of PTM could hinder the self-doped oxidization of Sn^{2+} to Sn^{4+} within the sample. The $CsSnI_3$-PTM sample also exhibited higher thermal stability (maintains 58.9% of its initial weight at 330 ºC) as compared to the $CsSnI_3$ sample (retains 53.9% of its initial weight at 330 ºC). The phase transition temperature from precursor to B-γ $CsSnI_3$ was reduced from ~70 ºC of bare $CsSnI_3$ sample to ~64 ºC of $CsSnI_3$-PTM sample, as shown by the differential scanning calorimetry (DSC) results in Supplementary Fig. 17.

These advantages provided by PTM originate from the trigeminal coordination between Sn^{2+} in $CsSnI_3$ and the NH as well as two CO units in PTM. Strong coordination interactions can be formed when the lone electron pairs of the NH unit are delocalized to the 5p empty orbitals of Sn^{2+} ($4d^{10}5s^2$) in $CsSnI_3$,[28,37] and the lone electron pairs of the two relatively far CO units of PTM can form weak coordination interactions with the Sn^{2+} in $CsSnI_3$. To verify this mechanism, various characterizations were conducted to quantify the chemical interactions. The remarkable cyclic voltammetry (CV) scan difference (Supplementary Fig. 18) between $CsSnI_3$ and $CsSnI_3$-PTM indicated that the PTM could form coordination bonding with the $CsSnI_3$. The Fourier transform infrared (FTIR) spectroscopy measurements provided the information on chemical interactions between the PTM and $CsSnI_3$, as shown in Figs. 2a-2c (the full spectra can be found in Supplementary Fig. 19). The NH stretching vibration (Fig. 2a) of the PTM sample was identified at 3206 cm^{-1}, which showed a shift to 3202 cm^{-1} for the $CsSnI_3$-PTM sample. The NH bending vibration (Fig. 2b) at 1606 cm^{-1} was measured for the PTM molecule, which shifted to 1598 cm^{-1} in the $CsSnI_3$-PTM sample. The CO stretching vibration (Fig. 2c) was located at 1755 cm^{-1} of the PTM sample and it shifted to 1747 cm^{-1} in the $CsSnI_3$-PTM sample. The infrared peak variations demonstrate that PTM was not only physically absorbed on the surface of $CsSnI_3$, but also chemically interacted with $CsSnI_3$ through the NH and two CO units. Fig. 2d shows the ^{119}Sn NMR spectra[38] for the $CsSnI_3$ and $CsSnI_3$-PTM samples prepared with dimethyl sulfoxide-d_6 (DMSO-d_6) as solvent. A chemical shift from -616.99 ppm of plain $CsSnI_3$ sample to -616.21 ppm of $CsSnI_3$-PTM sample can be found in the ^{119}Sn NMR spectra, indicating that Sn

should be the active site within $CsSnI_3$ and the electron density of Sn is increased. In ^1H NMR spectra (Supplementary Figs. 20 and 21) of the neat PTM sample, the resonance signal attributes to the NH (Fig. 2e) units, appearing at $\delta = 11.32$ ppm. The resonance signal showed an overall chemical shift of $\Delta\delta \approx 0.23$ ppm to 11.09 ppm for the $CsSnI_3$-PTM sample, revealing that the chemical interaction between NH group and $CsSnI_3$. Furthermore, ^{13}C NMR results (Supplementary Figs. 22 and 23) showed that the resonance signal of $\delta = 169.40$ ppm arising from the CO group (Fig. 2f) in PTM underwent a chemical shift of $\Delta\delta \approx 0.28$ ppm to $\delta = 169.68$ ppm for the $CsSnI_3$-PTM sample. Such variations of PTM molecular structure further verified the occurance of the chemical interactions between the CO group of PTM and perovskite. Next, XPS measurements were conducted to investigate the chemical interactions between the PTM and $CsSnI_3$. The full XPS spectra of the PTM, $CsSnI_3$, and $CsSnI_3$-PTM samples are shown in Supplementary Fig. 24. The Sn $3d_{5/2}$ XPS spectra in Fig. 2g further confirmed that the Sn from $CsSnI_3$ should be the active site to coordinate with the NH and CO units in PTM since the peak binding energy of the Sn $3d_{5/2}$ spectrum exhibited a clear shift towards lower binding energy (~0.1 eV) from $CsSnI_3$ to $CsSnI_3$-PTM while the differences of Cs $3d_{5/2}$ and I $3d_{5/2}$ XPS spectra between $CsSnI_3$ and $CsSnI_3$-PTM samples were not remarkable, as shown in Fig. 2h and Supplementary Fig. 25. It is noteworthy that the proportion of Sn^{4+} was much reduced in the $CsSnI_3$-PTM sample, indicating that the self-doping of Sn^{2+} to Sn^{4+} has been significantly restrained.[18] Generally, the defect density of $CsSnI_3$ is strongly associated with the density of Sn^{4+}.[7,8,11,18,39] These results indicate that the device fabricated using PTM modified

$CsSnI_3$ light absorber with lower defect density will exhibit promising performance. Fig. 2i shows the O 1s XPS spectra for the PTM and $CsSnI_3$-PTM samples and a clear fitted CO peak shift towards lower binding energy and a small fitted peak can be observed after the formation of the coordination bonding (adjusting of localized electron density) between CO units and $CsSnI_3$. A small fitted peak also can be found in the N 1s XPS spectra of $CsSnI_3$-PTM sample (Supplementary Fig. 26), indicating that the coordination bonding between NH units and $CsSnI_3$. These FTIR, NMR, and XPS results indicate that the chemical environment (localized electron density) of Sn can be increased *via* the lone electron pairs from the functional groups (NH and CO) within PTM. Apart from the common fragile single-site coordination[17,18] between additives and $CsSnI_3$, the proposed trigeminal coordination approach that engages one main coordination site (NH) with two symmetrical active sites (CO) is shown to provide more effective increase in the electron density around the Sn^{2+} offering excellent protection from oxidation to Sn^{4+}.

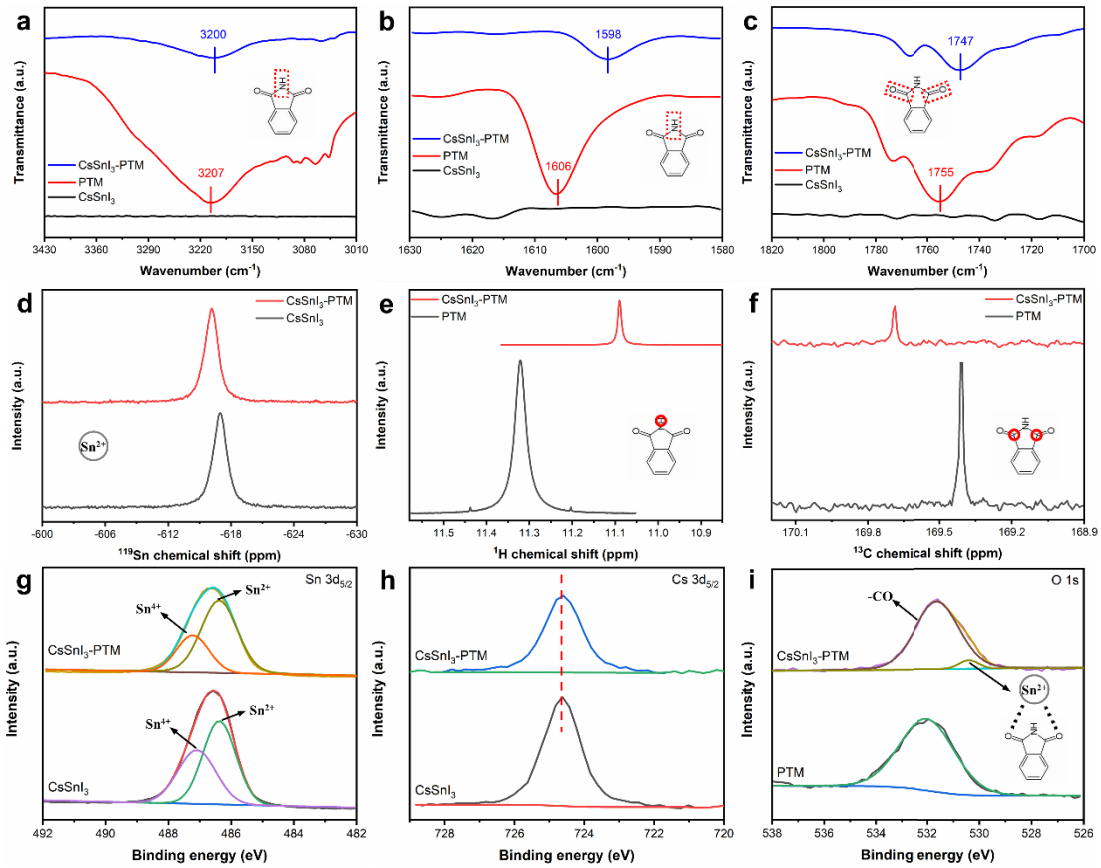

Fig. 2. The trigeminal coordination interactions between PTM and $CsSnI_3$. FTIR spectra of (**a**) NH stretching vibration, (**b**) NH bending vibration, and (**c**) CO stretching vibration for the $CsSnI_3$, $CsSnI_3$-PTM and PTM samples, respectively. (**d**) ^{119}Sn NMR spectra of $CsSnI_3$ and $CsSnI_3$-PTM samples in deuterated DMSO-d_6 solution. (**e**) ^{1}H NMR (NH) spectra of $CsSnI_3$-PTM and PTM samples in deuterated DMSO-d_6 solution. (**f**) ^{13}C NMR (CO) spectra of $CsSnI_3$-PTM and PTM samples in deuterated DMSO-d_6 solution. (**g**) XPS Sn $3d_{5/2}$ spectra of $CsSnI_3$ and $CsSnI_3$-PTM samples. (**h**) XPS Cs $3d_{5/2}$ spectra of $CsSnI_3$ and $CsSnI_3$-PTM samples. (**i**) XPS O 1s spectra of PTM and $CsSnI_3$-PTM samples.

The electron density differences and density of states (DOSs) for the PTM, $CsSnI_3$ and $CsSnI_3$-PTM samples have been simulated with DFT methods.[7,37,40-45] B-γ $CsSnI_3$

exhibits an orthorhombic structure with the Pnma space group symmetry. The optimized lattice parameters (a = 8.93 Å, b = 12.67 Å, and c = 9.05 Å) of the B-γ $CsSnI_3$ were similar to the experimental parameters (a = 8.69 Å, b = 12.38 Å, and c = 8.64 Å).[5,7] According to the XRD results, the (202) surface of B-γ $CsSnI_3$ is preferentially exposed after the addition of PTM, so it is cleaved in the DFT simulations. The adsorption energy of a PTM molecule on the (202) facet was calculated to be -0.45 eV. Fig. 3a-3c show the electron density differences of the $(CO)_2NH$ unit of a PTM molecule, Sn element of the $CsSnI_3$, and $(CO)_2NH$-Sn unit of $CsSnI_3$-PTM with same isovalues (± 0.03 e $Å^{-3}$) for the isosurface. The red dotted area in Fig. 3c clearly shows two regions of electron density change; the blue region indicates that the electron accumulation around Sn and the yellow region indicates that the electron depletion of the PTM. This provides the visualization for the strong coordination bonding between PTM and $CsSnI_3$. The partial DOS (PDOS) spectra of Sn in plain $CsSnI_3$ and $CsSnI_3$-PTM are shown in Fig. 3d. After the PTM is adsorbed on the (202) surface of $CsSnI_3$, the s and p orbital PDOSs of Sn (referred as sSn and pSn) vary in a large energy range (2-9 eV), indicating that the electronic environment of the Sn has been remarkably tuned. Fig. 3e shows that the sH (NH) is significantly changed when the PTM is adsorbed on the (202) surface of $CsSnI_3$. The sH (NH) is heavily overlapped with PDOSs of Sn within the $CsSbI_3$-PTM, indicating that strong coordination bonding between H (NH) and Sn is formed (the DOSs results of N are shown in Supplementary Fig. 27). Also, the PDOSs of two O (CO) are slightly different when the PTM is adsorbed on the (202) surface of $CsSnI_3$ and the PDOSs of both O^1 and O^2 are

overlapped with the PDOSs of Sn within the $CsSbI_3$-PTM, as shown in Figs. 3f and 3g, revealing the existence of coordination interactions between the two O (CO) and Sn. Interestingly, the PDOSs of the symmetrical O^1 and O^2 are nearly identical within the pure PTM molecule, while they are quite different in the $CsSnI_3$-PTM sample (as presented in Supplementary Figs. 28 and 29), exhibiting the self-adjusting behavior of the three functional units in PTM (with NH holding the primary coordinating position and two identical CO adjusting the suitable secondary positions). The total DOS patterns of the samples are presented in Supplementary Figs. 30 and 31.

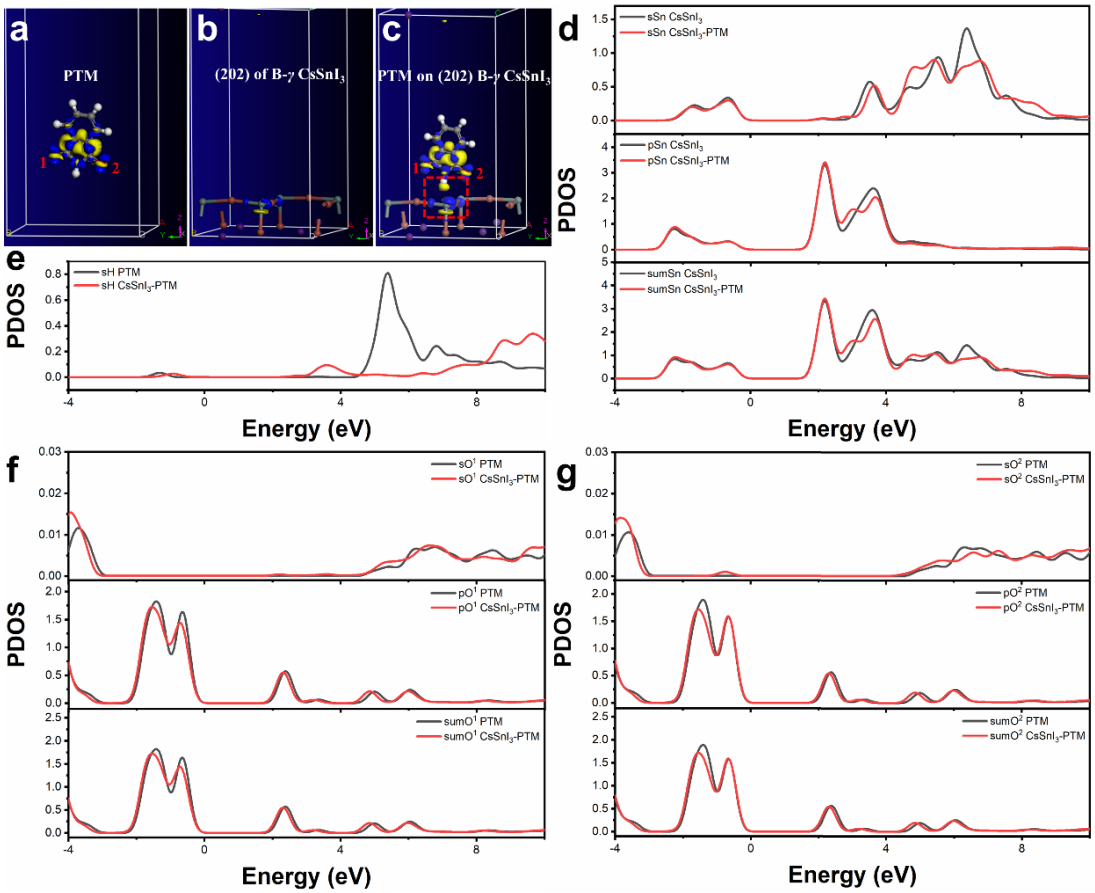

Fig. 3. DFT simulations. (**a**) Electron density difference of $(CO)_2NH$ structural unit within a PTM molecule. (**b**) Electron density difference of a Sn element on the (202)

surface of $CsSnI_3$. (**c**) Electron density difference of $(CO)_2NH$-Sn structural unit when a PTM molecule was adsorbed on the (202) surface of $CsSnI_3$. In (**a**-**c**), the isovalues for the isosurface is ± 0.03 e $Å^{-3}$. DFT-calculated PDOS profiles of (**d**) Sn, (**e**) H, (**f**) O^1, and (**g**) O^2 before and after adsorption of PTM on the (202) surface of $CsSnI_3$.

Inverted PSCs were fabricated with a configuration of: ITO/poly (3,4-ethylenedioxythiophene) polystyrene sulfonate (PEDOT:PSS)/perovskite/indene-C_{60} bisadduct (ICBA)/BCP/Ag (The detailed fabrication process can be found in Materials and Methods section in Supporting Information). ICBA used here due to the suitable band energy alignment with the Sn-based perovskite film.[22] The cross-section SEM images of the PSCs fabricated with $CsSnI_3$ and $CsSnI_3$-PTM are shown in Fig. 4a and 4b. Functional layers in the $CsSnI_3$-PTM device were compact, which agrees well with the surface SEM images (Fig. 1d). The PCE of PSCs increased gradually with the increase of PTM addition amount and reached the peak for $CsSnI_3$-3.0 devices, then decreased with more PTM added into the system, as shown in Fig. 4c. Fig. 4d shows the current density-voltage (*J-V*) characteristics for the small area (0.08 cm^2) $CsSnI_3$ and $CsSnI_3$-PTM devices under simulated air mass (AM) 1.5G radiation. The $CsSnI_3$-PTM device exhibited an overall PCE of 10.1% with open-circuit voltage (V_{oc}) of 0.64 V, short-circuit current density (J_{sc}) of 21.81 mA cm^{-2} and fill factor (*FF*) of 0.721 (the PCEs of the state-of-the-art Sn-based PSCs can be found in Supplementary Table 3). In comparison, the PCE for $CsSnI_3$ device was 5.5%, with V_{oc} of 0.47 V, J_{sc} of 18.09 mA cm^{-2} and *FF* of 0.648. The hysteresis between the forward (FW) and backward (BW)

scans for the $CsSnI_3$-PTM device was small, as demonstrated in Supplementary Fig. 32. The V_{oc} enhancement from $CsSnI_3$ device to $CsSnI_3$-PTM was derived from the reduced trap density within the light absorber after the incorporation of PTM by suppressing self-doping of Sn^{2+} to Sn^{4+}. As compared to other results,[8,18] the V_{oc} enhancement of the $CsSnI_3$-based devices could be ascribed to the timely removing of the solvent vapor during the device fabrication within the glovebox.[39] It is worth noted that the V_{oc} of all the PSCs is relatively low as compared to the bandgap of the B-γ $CsSnI_3$ which may originate from the defects (Sn^{4+}) within the perovskite films,[14,22] so the PCE of the $CsSnI_3$ based PSCs can be further improved by fine-tuning the perovskite light absorbers. The incident photon-to-electron conversion efficiency (IPCE) spectra of the $CsSnI_3$ and $CsSnI_3$-PTM devices are shown in Fig. 4e. The integrated current values were 21.45 and 17.05 mA cm^{-2} for the $CsSnI_3$-PTM and $CsSnI_3$ devices, respectively, which agrees closely with the J_{sc} values extracted from *J-V* characteristics. The IPCE enhancement at longer wavelength of the $CsSnI_3$-PTM could be ascribed to the higher optical absorption at this region and better film quality formed after the incorporation of PTM (will be discussed later). It should be noted that the IPCE extended to ~970 nm due to the shallow defects within the perovskite films.[4,7,10, 31,39] The steady-state output of the $CsSnI_3$-PTM device at maximum power point (MPP)[46,47] is shown in Fig. 4f. It exhibited a stable efficiency of 9.7% within a 5 min period. Furthermore, the suitability of the $CsSnI_3$-PTM film for large-area (1 cm^2) device fabrication has been explored, as shown in Fig. 4g. PCEs of 7.3% and 7.8% were extracted from the FW and BW *J-V* scans for the large-area rigid $CsSnI_3$-PTM device (histogram of PCEs for 25 devices

can be seen in Supplementary Fig. 33).

To check the suitability of $CsSnI_3$-PTM film for flexible device fabrication, the rigid ITO glass substrate was replaced by ITO polyethylene naphthalate (PEN) substrate but the deposition methods for other functional layers were kept identical to that for rigid device. Supplementary Fig. 34a shows the FW and BW *J-V* curves of the small-area (0.08 cm^2) $CsSnI_3$-PTM flexible device. PCEs of 9.4% and 9.3% were obtained for the FW and BW scans, respectively (histogram of PCEs for 25 devices can be seen in Supplementary Fig. 35). With regards to large-area (1 cm^2) $CsSnI_3$-PTM flexible device (Supplementary Fig. 34b), the PCEs of 6.2% and 6.6% were extracted from the FW and BW *J-V* scans, respectively (histogram of PCEs for 25 devices can be seen in Supplementary Fig. 36). The mechanical stability of the flexible device was also investigated, as shown in Supplementary Fig. 34c. The $CsSnI_3$-PTM device retained ~77% of its original PCE after 2000 times of small radius (4 mm) bending cycles. These results indicate that the $CsSnI_3$-PTM film offers a good choice for flexible device fabrication. The applicability of the localized electron density enhancement strategy through PTM incorporation was further confirmed within the $FASnI_3$ (where FA is formamidinium) PSCs, and the photovoltaic results could be found in Supplementary Figs. 37-39 and Supplementary Note 4.

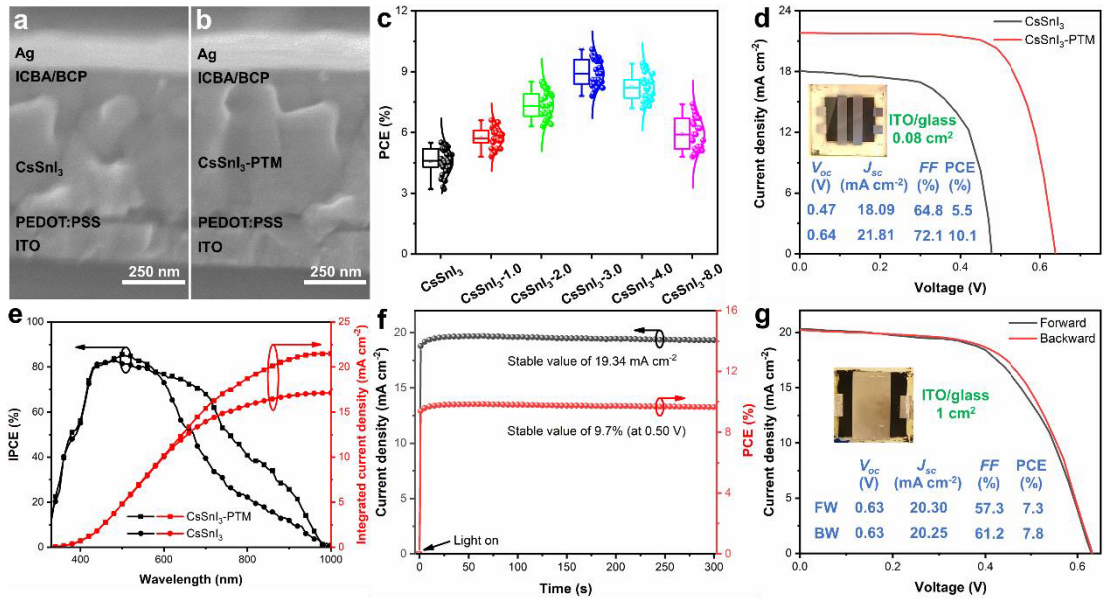

Fig. 4. Photovoltaic performances of PSCs. Cross-section SEM images of (**a**) $CsSnI_3$ and (**b**) $CsSnI_3$-PTM PSCs, respectively. (**c**) PCE distribution of the 0.08 cm^2 rigid PSCs fabricated with precursor solutions with different amounts of PTM and the reference devices (25 devices for each group). (**d**) *J-V* curves of the small-area champion rigid PSCs fabricated with $CsSnI_3$ and $CsSnI_3$-PTM films under simulated AM 1.5G radiation. (**e**) IPCE spectra and integrated current densities of the rigid PSCs fabricated with $CsSnI_3$ and $CsSnI_3$-PTM films. (**f**) Steady-state MPP output of the rigid $CsSnI_3$-PTM PSC. (**g**) *J-V* curves (FW and BW scans) of the large-area champion rigid $CsSnI_3$-PTM PSC under simulated AM 1.5G radiation. All insets show the real images of the PSCs used for *J-V* measurements or bending tests.

In order to understand the photogenerated hole injection/transport mechanism within the device structure, an ITO glass/PEDOT:PSS/perovskite sample was fabricated. Fig. 5a shows the PL spectra of the $CsSnI_3$ and $CsSnI_3$-PTM samples with the light irradiating from the ITO side. A significantly reduced PL peak intensity has been

recorded for the $CsSnI_3$-PTM sample, indicating that faster hole extraction/transport within the sample. Supplementary Fig. 40 shows the TRPL spectra of the ITO glass/PEDOT:PSS/perovskite samples. The PL decay lifetime was calculated to be 1.14 ns for the $CsSnI_3$ sample, while it decreased to only 0.53 ns for the $CsSnI_3$-PTM sample, indicating that the photogenerated holes in the ITO glass/PEDOT:PSS/$CsSnI_3$-PTM sample were efficiently extracted from perovskite film into PEDOT:PSS layer with reduced non-radiative recombination loss.[33] Therefore, the PL results obtained from bare perovskite films and HTM/perovskite heterojunctions demonstrated that the PTM addition would not only reduce the defect density within the perovskite film, but also improve the photogenerated hole extraction/transport at the HTM/perovskite interface.

The hole-only devices with a configuration of ITO glass/PEDOT:PSS/perovskite (with and without PTM)/Au were fabricated to calculate the trap density of $CsSnI_3$ and $CsSnI_3$-PTM samples. Fig. 5b shows *J-V* curves of the hole-only devices measured under the dark condition. An ohmic response within low bias region is obtained since the linear correlation between current and bias voltage. Traps are filled by injected carriers (nonlinear increase of current) when the applied voltage increases above the trap-filled limit voltage (V_{TFL}).[33,48] The hole trap density of the $CsSnI_3$ film was estimated to be 3.88×10^{15} cm^{-3}. After the incorporation of PTM, the hole trap density was reduced to 3.15×10^{15} cm^{-3} (Supplementary Fig. 41 and Supplementary Note 5). The current exhibits a quadratic relationship with voltage in the high bias region. The hole mobilities of the $CsSnI_3$ and $CsSnI_3$-PTM films were calculated as 2.40 cm^2 V^{-1} s^{-}

^{1} and 5.91 cm^2 V^{-1} s^{-1}, respectively (Supplementary Note 5). The later hole mobility value of $CsSnI_3$-PTM film is consistent with the hole mobility value of 6.21 cm^2 V^{-1} s^{-1} measured with Hall effect measurement.[4] The electron-only devices with a configuration of ITO glass/SnO_2/perovskite (with and without PTM)/Ag were fabricated to calculate the electron trap density of $CsSnI_3$ and $CsSnI_3$-PTM samples. The electron trap densities of the $CsSnI_3$ and $CsSnI_3$-PTM film were estimated to be 4.02×10^{15} cm^{-3} and 3.18×10^{15} cm^{-3}, respectively (Supplementary Fig. 42). The electron mobilities of the $CsSnI_3$ and $CsSnI_3$-PTM films were calculated as 5.60 cm^2 V^{-1} s^{-1} and 7.63 cm^2 V^{-1} s^{-1}, respectively. Thus, the small amount of PTM addition assisted the formation of B-γ $CsSnI_3$ film with reduced trap density and enhanced charge mobility.

Electrochemical impedance spectroscopy (EIS) was conducted to quantify the charge transfer and recombination dynamics in the devices. Fig. 5c shows the Nyquist plots and the equivalent circuit model of the $CsSnI_3$ and $CsSnI_3$-PTM solar cells measured under dark condition at V_{oc}. The corresponding fitting parameters are listed in Supplementary Table 4. After the insertion of the PTM, the recombination resistance (R_{rec})[33,49] was significantly increased from 996 Ω to 1790 Ω, indicating that the defect passivation by reducing Sn^{4+} content through PTM modification suppresses charge recombination. These results suggest that the charge carrier recombination within the $CsSnI_3$-PTM PSC was effectively reduced with the decrease in defect density.

The stabilities of the perovskite films with and without PTM incorporation, and corresponding devices were tested under different conditions, including inert, ambient, MPP operation under continuous 1 Sun illumination in ambient at 70 ^{o}C. Supplementary Fig. 43 shows the precursor solution aging results for the as-prepared $CsSnI_3$ and $CsSnI_3$-PTM solutions under ambient atmosphere at RT. It is obvious that the clear plain $CsSnI_3$ solution gradually turns to muddy, which means increasing oxidation of Sn^{2+} to Sn^{4+} in the solution, while the $CsSnI_3$-PTM solution keeps clear and remains its original color. The real images of devices in Supplementary Fig. 44 reflect the color/transparency evolution of the $CsSnI_3$ and $CsSnI_3$-PTM devices. The $CsSnI_3$-PTM device kept its original dense black nature after 10 days of ambient-air exposure, while the $CsSnI_3$ device gradually became slightly transparent during the same period under identical condition. Supplementary Fig. 45 shows the water contact angle results of the $CsSnI_3$ and $CsSnI_3$-PTM films, which suggest that the PTM addition increases the water contact angle from 55.2^{o} of $CsSnI_3$ film to 72.4^{o} of $CsSnI_3$-PTM film. This implies that the incorporation of PTM may increase the ambient air stability of the $CsSnI_3$-PTM devices. Supplementary Fig. 46 shows the evolution of normalized absorbance at 500 nm for the $CsSnI_3$ and $CsSnI_3$-PTM films within a 1 h of continuous measurement.[6] The intensity change of the $CsSnI_3$-PTM film was negligible while it reduced gradually for the $CsSnI_3$ sample and just retained ~81% of its initial value after 1 h of ambient-air exposure (the full spectra can be found in Supplementary Figs. 47 and 48). It should be noted that the $CsSnI_3$ grain was found to degrade from edge area after the TEM sample was placed in ambient atmosphere, reflected by the obscure

lattice fringes in Supplementary Figs. 49 and 50. The crystal features of CsI and Cs_2SnI_6 were observed during the air-exposure process (Supplementary Figs. 49-51). Negligible crystal grain degradation was observed for the $CsSnI_3$-PTM system during the identical ambient atmosphere exposure periods (Supplementary Figs. 52-54), indicating that the thin layer of PTM protected the perovskite crystal grain from degradation.[28] Next, both inert and ambient-air stabilities of the encapsulated PSCs were investigated. The encapsulated devices were stored under inert condition (RT) for 60 days and the average PCE of the PTM modified devices slightly decreased to 94.3% of their original value after the storage. However, the average PCE of the $CsSnI_3$ devices remarkably decreased to merely 73.5% during the same period (Fig. 5d). With regards to devices stored under ambient condition (RT and 30% relative humidity) for 45 days, the average PCE of the $CsSnI_3$ devices decreased to 59.5% of their original PCE while the $CsSnI_3$-PTM devices maintained 83.4% of their original PCE (Fig. 5e). When an encapsulated $CsSnI_3$-PTM device was placed more severe conditions (1 Sun continuous illumination in ambient atmosphere with 30% relative humidity at 70 ^oC), it maintained 81.3% of its initial PCE after 2000 min of MPP operation, while the encapsulated $CsSnI_3$ device retained only 63.2% of its initial PCE under the same condition, as illustrated in Fig. 5f. Thus, the incorporation of PTM in the $CsSnI_3$ not only improves the PCE of the device but also enhances both inert and ambient-air stability of the PSC (the stabilities of the state-of-the-art Sn-based PSCs can be found in Supplementary Table 3). The extra benefit of $CsSnI_3$ over $FASnI_3$ is the higher thermal and moisture stability, as the device and film stability results shown in Supplementary Figs. 55-58 and Supplementary Note

6.

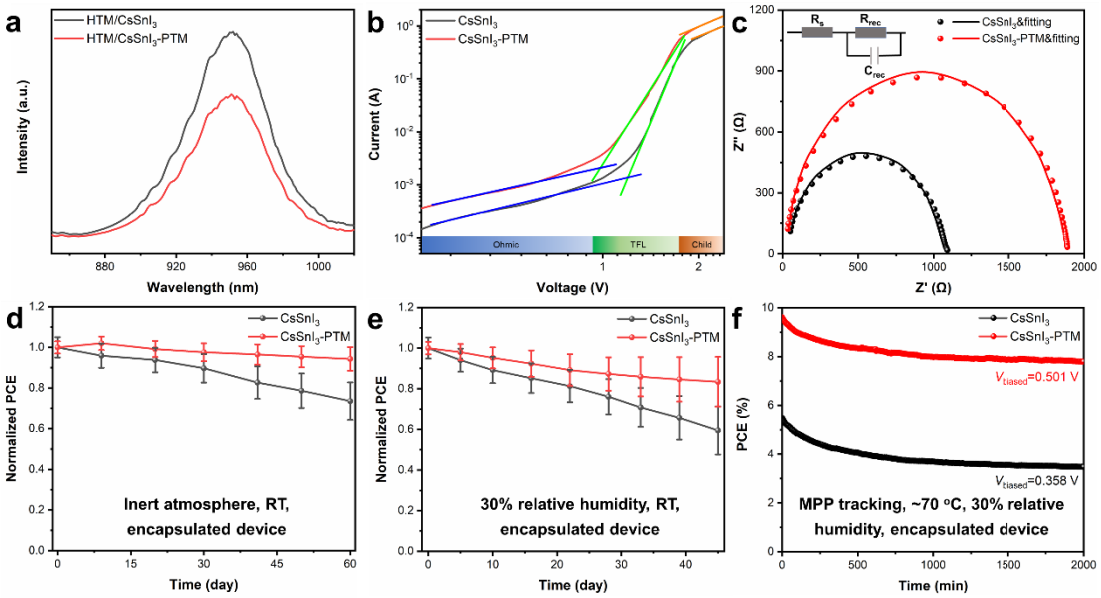

Fig. 5. Charge carrier dynamics and stability of the PSCs. (**a**) Steady-state PL spectra of ITO/PEDOT:PSS/$CsSnI_3$ and ITO/PEDOT:PSS/$CsSnI_3$-PTM samples, Xenon light was irradiated on the ITO side. (**b**) *J-V* curves of the hole-only devices fabricated with $CsSnI_3$ and $CsSnI_3$-PTM films measured under dark condition and the data is fitted by space-charge limited current (SCLC) model. (**c**) Nyquist plots of $CsSnI_3$ and $CsSnI_3$-PTM based PSCs measured at V_{oc} under dark condition, inset is the equivalent circuit employed to fit the plots. Stability measurements on the encapsulated $CsSnI_3$ and $CsSnI_3$-PTM PSCs under (**d**) inert RT (12 devices for each group) and (**e**) ambient atmosphere with 30% relative humidity RT (12 devices for each group) respectively. (**f**) MPP tracking results of the encapsulated $CsSnI_3$ and $CsSnI_3$-PTM PSCs under 1 Sun continuous illumination and ambient atmosphere with 30% relative humidity at ~70 °C.

This study demonstrates localized electron density engineering strategy to stabilize the fully-inorganic lead-free B-γ $CsSnI_3$ by incorporating PTM with trigeminal functional groups. Through systematic experimental measurements and theoretical calculations, we found that the lone electron pairs of NH and two CO functional groups in the PTM enhances the electron density around the Sn^{2+} within the $CsSnI_3$ and protects it from oxidation to Sn^{4+}. This results in low defect density and highly stable $CsSnI_3$-PTM film. After modification, the highest PCEs of 10.1% and 7.8% were documented for the 0.08 cm^2 and 1.0 cm^2 rigid ITO glass-based PSCs, respectively. The PCEs of 9.6% and 6.6% were recorded for the 0.08 cm^2 and 1.0 cm^2 flexible ITO PEN-based PSCs, respectively. Results show that the strong trigeminal coordination bonding between PTM and $CsSnI_3$ stabilized the B-γ $CsPbI_3$ grains under virous conditions. The PTM modified devices sustained 94.3%, 83.4% and 81.3% of their initial PCE after 60 days of storage in inert condition (RT), 45 days of storage in ambient condition (RT and 30% relative humidity), and 2000 min of MPP operation under 1 Sun continuous illumination in ambient at 70 ^oC, respectively. These results provide a transformative solution for the realization of highly efficient and stable B-γ $CsSnI_3$ PSCs.

Supporting Information

The Supporting Information is available free of charge on the ACS Publications website at xx. Experimental section, SEM, UV-vis spectrum, Tauc plot of optical absorption, PL/TRPL, XRD, TEM, HAADF-STEM, EDS, NMR, FTIR, XPS, device performance, SCLC, EIS, images, water contact angle, simulated crystal details, DFT simulation

results.

Author Information

*****Corresponding author. Email: tvy5161@psu.edu; sup103@psu.edu.

Notes

The authors declare no conflicts of interests.

Acknowledgments

T.Y. acknowledges the financial support from Nanosonic Inc. (STTR). K.W. acknowledges the financial support from office of naval research through grant number N000141912461. S.M. acknowledges the financial support from the Fundamental Research Funds for the Central Universities through grant number 2020RC017. D.Y. acknowledges the financial support from NSF I/UCRC: Center for Energy Harvesting Materials and Systems (CEHMS). Y.C. acknowledges financial support from DARPA through grant number HR00111920001. J.Y. acknowledges the financial support from Army RIF program. S.P. acknowledges the financial support from National Science Foundation through award number 1936432.

References

1. Abate, A. J. J. Perovskite solar cells go lead free. *Joule* **2017**, *1*, 659-664.

2. Correa-Baena, J. P.; Saliba, M.; Buonassisi, T.; Grätzel, M.; Abate, A.; Tress, W.; Hagfeldt, A. Promises and challenges of perovskite solar cells. *Science* **2017**, *358*, 739-744.

3. Babayigit, A.; Ethirajan, A.; Muller, M.; Conings, B. Toxicity of organometal halide

perovskite solar cells. *Nat. Mater.* **2016**, *15*, 247-251.

4. Kumar, M. H.; Dharani, S.; Leong, W. L.; Boix, P. P.; Prabhakar, R. R.; Baikie, T.; Shi, C.; Ding, H.; Ramesh, R.; Asta, M.; Graetzel, M. Mhaisalkar, S. G.; Mathews, N. Lead-free halide perovskite solar cells with high photocurrents realized through vacancy modulation. *Adv. Mater.* **2014,** *26*, 7122-7127.

5. Stoumpos, C. C.; Malliakas, C. D.; Kanatzidis, M. G. Semiconducting tin and lead iodide perovskites with organic cations: phase transitions, high mobilities, and near-infrared photoluminescent properties. *Inorg. Chem.* **2013**, *52*, 9019-9038.

6. Marshall, K. P.; Walker, M.; Walton, R. I.; Hatton, R. A. Enhanced stability and efficiency in hole-transport-layer-free $CsSnI_3$ perovskite photovoltaics. *Nat. Energy* **2016,** *1*, 16178.

7. Chung, I.; Song, J. H.; Im, J.; Androulakis, J.; Malliakas, C. D.; Li, H.; Freeman, A. J.; Kenney, J. T.; Kanatzidis, M. G. $CsSnI_3$: semiconductor or metal? high electrical conductivity and strong near-infrared photoluminescence from a single material. high hole mobility and phase-transitions. *J. Am. Chem. Soc.* **2012**, *134*, 8579-8587.

8. Wang, N.; Zhou, Y.; Ju, M. G.; Garces, H. F.; Ding, T.; Pang, S.; Zeng, X. C.; Padture, N. P.; Sun, X. W. Heterojunction-depleted lead-free perovskite solar cells with coarse-grained B-γ-$CsSnI_3$ thin films. *Adv. Energy Mater.* **2016**, *6*, 1601130.

9. Shum K.; Tsatskina, A. Solar cells: stabilizing tin-based perovskites. *Nat. Energy* **2016**, *1*, 16188.

10. Wu, B.; Zhou, Y.; Xing, G.; Xu, Q.; Garces, H. F.; Solanki, A.; Goh, T. W.; Padture, N. P.; Sum, T. C. Long minority‐carrier diffusion length and low surface‐

recombination velocity in inorganic lead-free $CsSnI_3$ perovskite crystal for solar cells. *Adv. Funct. Mater.* **2017**, *27*, 1604818.

11. Tai, Q.; Guo, X.; Tang, G.; You, P.; Ng, T. W.; Shen, D.; Cao, J.; Liu, C. K.; Wang, N.; Zhu, Y.; Lee, C. S.; Yan, F. Antioxidant grain passivation for air-stable tin-based perovskite solar cells. *Angew. Chem. Int. Ed.* **2019**, *58*, 806-810.

12. Chung, I.; Lee, B.; He, J.; Chang, R. P.; Kanatzidis, M. G. All-solid-state dye-sensitized solar cells with high efficiency. *Nature* **2012**, *485*, 486-489.

13. Chen, Z.; Wang, J. J.; Ren, Y.; Yu, C.; Shum, K. Schottky solar cells based on $CsSnI_3$ thin-films. *Appl. Phys. Lett.* **2012**, *101*, 093901.

14. Ma, S.; Gu, X.; Kyaw, A. K. K.; Wang, D. H.; Priya, S.; Ye, T. Fully inorganic $CsSnI_3$-based solar cells with > 6% efficiency and enhanced stability enabled by mixed electron transport layer. *ACS Appl. Mater. Interfaces* **2021**, *13*, 1345-1352.

15. Kontos, A. G.; Kaltzoglou, A.; Siranidi, E.; Palles, D.; Angeli, G. K.; Arfanis, M. K.; Psycharis, V.; Raptis, Y. S.; Kamitsos, E. I.; Trikalitis, P. N.; Stoumpos, C. C. Structural stability, vibrational properties, and photoluminescence in $CsSnI_3$ perovskite upon the addition of SnF_2. *Inorg. Chem.* **2017**, *56*, 84-91.

16. Li, B.; Di, H.; Chang, B.; Yin, R.; Fu, L.; Zhang, Y. N.; Yin, L. Efficient passivation strategy on Sn related defects for high performance all-inorganic $CsSnI_3$ perovskite solar cells. *Adv. Funct. Mater.* **2021**, *31*, 2007447.

17. Zhang, T.; Li, H.; Ban, H.; Sun, Q.; Shen, Y.; Wang, M. Efficient $CsSnI_3$-based inorganic perovskite solar cells based on a mesoscopic metal oxide framework *via* incorporating a donor element. *J. Mater. Chem. A* **2020**, *8*, 4118-4124.

18. Wang, Y.; Tu, J.; Li, T.; Tao, C.; Deng, X.; Li, Z. Convenient preparation of $CsSnI_3$ quantum dots, excellent stability, and the highest performance of lead-free inorganic perovskite solar cells so far. *J. Mater. Chem. A* **2019**, *7*, 7683-7690.

19. Kim, M.; Kim, G. H.; Lee, T. K.; Choi, I. W.; Choi, H. W.; Jo, Y.; Yoon, Y. J.; Kim, J. W.; Lee, J.; Huh, D.; Lee, H. Kwak, S. K.; Kim, J. Y.; Kim D. S. Methylammonium chloride induces intermediate phase stabilization for efficient perovskite solar cells. *Joule* **2019**, *3*, 2179-2192.

20. Jiang, Q.; Zhao, Y.; Zhang, X.; Yang, X.; Chen, Y.; Chu, Z.; Ye, Q.; Li, X.; Yin, Z.; You, J. Surface passivation of perovskite film for efficient solar cells. *Nat. Photon.* **2019**, *13*, 460-466.

21. National Renewable Energy Laboratory. *Best Research-Cell Efficiency Chart.* https://www.nrel.gov/pv/cell-efficiency.html (accessed 2021-02-15).

22. Jiang, X.; Wang, F.; Wei, Q.; Li, H.; Shang, Y.; Zhou, W.; Wang, C.; Cheng, P.; Chen, Q.; Chen, L.; Ning, Z. Ultra-high open-circuit voltage of tin perovskite solar cells *via* an electron transporting layer design. *Nat. Commun.* **2020**, *11*, 1245.

23. Nishimura, K.; Kamarudin, M.A.; Hirotani, D.; Hamada, K.; Shen, Q.; Iikubo, S.; Minemoto, T.; Yoshino, K.; Hayase, S. Lead-free tin-halide perovskite solar cells with 13% efficiency. *Nano Energy* **2020**, *74*, 104858.

24. Meng, X.; Wang, Y.; Lin, J.; Liu, X.; He, X.; Barbaud, J.; Wu, T.; Noda, T.; Yang, X.; Han, L. Surface-controlled oriented growth of $FASnI_3$ crystals for efficient lead-free perovskite solar cells. *Joule* **2020**, *4*, 902-912.

25. Ye, T.; Bruno, A.; Han, G.; Koh, T. M.; Li, J.; Jamaludin, N. F.; Soci, C.; Mhaisalkar,

S. G.; Leong, W. L. Efficient and ambient-air-stable solar cell with highly oriented 2D@3D perovskites. *Adv. Funct. Mater.* **2018**, *28*, 1801654.

26. Zheng, X.; Hou, Y.; Bao, C.; Yin, J.; Yuan, F.; Huang, Z.; Song, K.; Liu, J.; Troughton, J.; Gasparini, N.; Zhou, C.; Lin, Y.; Xue, D.-J. Chen, B.; Johnston, A. K.; Wei, N.; Hedhili, M. N.; Wei, M.; Alsalloum, A. Y.; Maity, P.; Turedi, B.; Yang, C.; Baran, D.; Anthopoulos, T. D.; Han, Y.; Lu, Z.-H.; Mohammed, O. F.; Gao, F.; Sargent E. H.; Bakr, O. M. Managing grains and interfaces *via* ligand anchoring enables 22.3%-efficiency inverted perovskite solar cells. *Nat. Energy* **2020** *5*, 131-140.

27. Marshall, K. P.; Walker, M.; Walton, R. I.; Hatton, R. A. Elucidating the role of the hole-extracting electrode on the stability and efficiency of inverted $CsSnI_3/C_{60}$ perovskite photovoltaics. *J. Mater. Chem. A* **2017**, *5*, 21836-21845.

28. Ye, T.; Zhou, B.; Zhan, F.; Yuan, F.; Ramakrishna, S.; Golberg, D.; Wang, X. Below 200 ^oC Fabrication strategy of black phase $CsPbI_3$ film for ambient-air-stable solar cells. *Sol. RRL* **2020**, *4*, 2000014.

29. Li, M.; Zuo, W. W.; Yang, Y. G.; Aldamasy, M. H.; Wang, Q.; Cruz, S. H. T.; Feng, S. L.; Saliba, M.; Wang, Z. K.; Abate, A. Tin halide perovskite films made of highly oriented 2D crystals enable more efficient and stable lead-free perovskite solar cells. *ACS Energy Lett.* **2020**, *5*, 1923-1929.

30. Bi, D.; Yi, C.; Luo, J.; Décoppet, J.D.; Zhang, F.; Zakeeruddin, S. M.; Li, X.; Hagfeldt, A.; Grätzel, M. Polymer-templated nucleation and crystal growth of perovskite films for solar cells with efficiency greater than 21%. *Nat. Energy* **2016**, *1*, 16142.

31. Song, T. -B.; Yokoyama, T.; Aramaki, S.; Kanatzidis, M. G. Performance enhancement of lead-free tin-based perovskite solar cells with reducing atmosphere-assisted dispersible additive. *ACS Energy Lett*. **2017,** *2*, 897-903.

32. Wagner, C.; Green, M. F.; Maiworm, M.; Leinen, P.; Esat, T.; Ferri, N.; Friedrich, N.; Findeisen, R.; Tkatchenko, A.; Temirov, R.; Tautz, F. S. Quantitative imaging of electric surface potentials with single-atom sensitivity. *Nat. Mater.* **2019**, *18*, 853-859.

33. Hou, Y.; Wu, C.; Yang, D.; Wang, K.; Ye, T.; Brownlie, L.; Wang, K.; Priya, S. Artemisinin (ART)-induced "perovskite/perovskite" bilayer structured photovoltaics. *Nano Energy* **2020**, *78*, 105133.

34. Yang, W. S.; Noh, J. H.; Jeon, N. J.; Kim, Y. C.; Ryu, S.; Seo, J.; Seok, S. I. High-performance photovoltaic perovskite layers fabricated through intramolecular exchange. *Science*, **2015**, *348*, 1234-1237.

35. Ng, C. H.; Nishimura, K.; Ito, N.; Hamada, K.; Hirotani, D.; Wang, Z.; Yang, F.; Shen, Q.; Yoshino, K.; Minemoto, T.; Hayase, S. Role of GeI_2 and SnF_2 additives for SnGe perovskite solar cells. *Nano Energy* **2019**, *58*, 130-137.

36. Leijtens, T.; Prasanna, R.; Gold-Parker, A.; Toney, M. F.; McGehee, M. D. Mechanism of tin oxidation and stabilization by lead substitution in tin halide perovskites. *ACS Energy Lett.* **2017**, *2*, 2159-2165.

37. Zuo, L.; Guo, H.; deQuilettes, D. W.; Jariwala, S.; De Marco, N.; Dong, S.; DeBlock, R.; Ginger, D. S.; Dunn, B.; Wang, M.; Yang, Y. Polymer-modified halide perovskite films for efficient and stable planar heterojunction solar cells. *Sci. Adv.* **2017**, *3*, e1700106.

38. Nakamura, T.; Yakumaru, S.; Truong, M.A.; Kim, K.; Liu, J.; Hu, S.; Otsuka, K.; Hashimoto, R.; Murdey, R.; Sasamori, T.; Kim, H. D.; Ohkita, H.; Handa, T.; Kanemitsu, Y.; Wakamiya, A. Sn(IV)-free tin perovskite films realized by in situ Sn(0) nanoparticle treatment of the precursor solution. *Nat. Commun.* **2020**, *11*, 3008.

39. Song, T. B.; Yokoyama, T.; Stoumpos, C. C.; Logsdon, J.; Cao, D. H.; Wasielewski, M. R.; Aramaki, S.; Kanatzidis, M. G. Importance of reducing vapor atmosphere in the fabrication of tin-based perovskite solar cells. *J. Am. Chem. Soc.* **2017**, *139*, 836-842.

40. Blöchl, P. E. Projector augmented-wave method. *Phys. Rev. B* **1994**, *50*, 17953-17979.

41. Kresse, G.; Furthmüller, J. Projector augmented-wave method. *Phys. Rev. B* **1996**, *54*, 11169-11186.

42. Kresse, G.; Joubert, D. From ultrasoft pseudopotentials to the projector augmented-wave method. *Phys. Rev. B* **1999**, *59*, 1758-1775.

43. Kresse, G.; Hafner, J. Ab initio molecular dynamics for liquid metals. *Phy. Rev. B* **1993**, *47*, 558-561.

44. Monkhorst, H. J.; Pack, J. D. Special points for Brillouin-zone integrations. *Phy. Rev. B* **1976**, *13*, 5188-5192.

45. Clark, S. J.; Segall, M. D.; Pickard, C. J.; Hasnip, P. J.; Probert, M. J.; Refson, K.; Payne, M. C. First principles methods using CASTEP. *Z. Kristallogr. Cryst. Mater.* **2005**, *220*, 567-570.

46. Ye, T.; Ma, S.; Jiang, X.; Wei, L.; Vijila, C.; Ramakrishna, S. Performance enhancement of tri-cation and dual-anion mixed perovskite solar cells by Au@SiO_2

nanoparticles. *Adv. Funct. Mater.* **2017**, *27*, 1606545.

47. Ran, C.; Gao, W.; Li, J.; Xi, J.; Li, L.; Dai, J.; Yang, Y.; Gao, X.; Dong, H.; Jiao, B.; Spanopoulos, I. Malliakas, C. D.; Hou, X.; Kanatzidis, M. G.; Wu, Z. Conjugated organic cations enable efficient self-healing $FASnI_3$ solar cells. *Joule* **2019**, *3*, 3072-3087.

48. Wang, R.; Xue, J.; Wang, K. L.; Wang, Z. K.; Luo, Y.; Fenning, D.; Xu, G.; Nuryyeva, S.; Huang, T.; Zhao, Y.; Yang, J. L.; Zhu, J.; Wang, M.; Tan, S.; Yavuz, I.; Houk, K. N.; Yang, Y. Constructive molecular configurations for surface-defect passivation of perovskite photovoltaics. *Science* **2019**, *366*, 1509-1513.

49. Tiwana, P.; Docampo, P.; Johnston, M. B.; Snaith, H. J.; Herz, L. M. Electron mobility and injection dynamics in mesoporous ZnO, SnO_2, and TiO_2 films used in dye-sensitized solar cells. *ACS Nano* **2011**, *5*, 5158-5166.